

Nonlinear management of the miscibility-immiscibility transition in binary Bose-Einstein condensates

B. B. Baizakov^{1,2}, B. A. Malomed^{3,4}, and M. Salerno⁵

¹ *Physical-Technical Institute, Uzbek Academy of Sciences, 100084, Tashkent, Uzbekistan,*

² *Institute of Theoretical Physics, National University of Uzbekistan, Tashkent 100174, Uzbekistan.*

³ *Department of Physical Electronics, School of Electrical Engineering, Faculty of Engineering, Tel Aviv University, Tel Aviv, 69978, Israel.*

⁴ *Instituto de Alta Investigación, Universidad de Tarapacá, Casilla 7D, Arica, Chile*

⁵ *Dipartimento di Fisica “E.R. Caianiello”, Università di Salerno, Via Giovanni Paolo II, 84084 Fisciano (SA), Italy,*

We investigate application of the nonlinearity management (NM, i.e., periodic variation of the strength of the inter-component repulsion) to the miscibility-immiscibility (MIM) transition across the critical point of a two-component BEC, both with and without the linear mixing (Rabi coupling, RC) between the components. To this end, we first identify, by means of a variational approximation and numerical solution, diverse stationary domain-wall (DW) structures supported by the system in the absence of the management. The approximate analytical solutions for the DWs are found to be in excellent agreement with their numerical counterparts. An analytical estimate is also produced for the upshift of the MIM transition caused by the pressure of the trapping potential in the case of a confined system. An exact DW solution is produced for the system including the Pöschl-Teller potential, which is stable (unstable) if the potential is repulsive (attractive). Further, we find the spectrum of linear excitations in the spatially uniform mixed state, and thus establish parameter regions where the system is stable/unstable against demixing. In particular, RC upshifts the critical strength of the inter-component repulsion for the onset of the MIM transition. Eigenfrequencies of excitations on top of DW states are identified from numerical simulations through monitoring the evolution of perturbed states. Weak NM applied at the DW eigenfrequency reveals features of the nonlinear resonance. Stronger NM, under which the system periodically crosses the MIM-transition point, restricts the miscibility.

PACS numbers:

I. INTRODUCTION

Two-component Bose-Einstein condensates (BECs) offer a platform for the realization of various static states and dynamical effects, in the form of matter waves. An adequate model of the two-component mixture is provided by the system of coupled Gross-Pitaevskii (GP) equations. In particular, a fundamentally important topic is the miscibility-immiscibility (MIM) transition in the binary condensate [1, 2]. In this case, the relation between scattering lengths of inter-atomic collisions, $a_{11,22}$, which determine the effective strengths of the self-repulsion in each component, and a_{12} , which determines the inter-component repulsion strength, plays a crucial role. In the spatially uniform binary condensate, the mixed state is unstable in the case of

$$\sqrt{a_{11}a_{22}} < a_{12}, \quad (1)$$

and is stable in the opposite case, while the demixed states, with spatially separated components, is stable in the former case, and unstable in the latter one [1, 3]. On the other hand, if a binary condensate is loaded in a potential trap, the pressure of the trapping potential naturally makes the BEC more miscible, upshifting the critical (demixing) value of a_{12} to one exceeding $\sqrt{a_{11}a_{22}}$ [4]. An example of this effect is briefly presented below, for the symmetric case, with $a_{11} = a_{22} \equiv a$: under the action of the trapping parabolic potential, it follows from Eq. (11) that the instability region (1) of the mixed states upshifts from $a < a_{12}$ to $a < (3/2)a_{12}$.

Using the Feshbach-resonance technique [6], binary condensates have been created with tunable inter-species interactions [7], which made it possible to demonstrate MIM phase transitions [5] and other effects, such as the creation of quantum droplets [8–10] and two-dimensional Townes solitons [11, 12]. A generic manifestation of the transition to immiscibility in two-component BECs is the formation of domain walls (DWs), i.e., boundaries separating immiscible components. The DW width is primarily determined by the strength of the inter-component repulsion. In terms of the underlying system of GP equations, DWs are represented by compound solutions which include a kink in one component and an antikink in the other (see, e.g., an exact DW solution given below by Eqs. (13) and (20)).

Apparently similar stationary DW patterns, alias *grain boundaries*, although maintained by different physical mechanisms, are commonly known in various forms in solid-state physics [13]–[16] and in magnetism [17, 18]. Another

realization of DW patterns is well known in the form of stationary quasi-one-dimensional boundaries between two-dimensional domains formed by mismatched phases that have a dynamical origin. These may be DWs produced by collision of propagating fronts in the framework of the Kibble-Zurek mechanism [19, 20], or boundaries between Rayleigh-Bénard-convection patterns of the roll type, with different orientations [21]-[26].

The formation of DWs in binary BECs, in connection to the MIM transitions in these systems, has been explored too, in diverse contexts [4, 27-29]. In addition to the empirical analysis reported in those works, a mathematically rigorous proof of the existence and stability of DWs, as stationary solutions of the respective system of nonlinearly-coupled GP equations, was elaborated too, including the system involving a weak localized potential acting on the binary condensate [30]. These findings suggest that there remain significant subjects for further studies of the MIM transitions and DWs in quasi-one-dimensional binary BECs. In this work, our first objective is to produce new analytical solutions for the DWs in binary BECs, taking into account the linear inter-conversion (Rabi coupling, RC) between the species. The RC gives rise to effective attraction between the immiscible components, therefore it essentially affects the respective MIM transition and DWs generated by it, which separate two *partially mixed* components. Further, by means of systematic numerical simulations we explore the stability of DWs against periodic variation of the strength of the inter-component repulsion (*nonlinearity management*, NM). The results are summarized in the form of a stability diagram for the DWs in the parameter plane of the NM strength and frequency. Our numerical analysis is performed, chiefly, in the ring-shaped system with periodic boundary conditions, of a sufficiently large length, with two DWs placed at diametrically opposite positions on the ring. The corresponding experimental setup can be a toroidal trap with strong radial confinement. In some cases, to explore the (in)stability of the analytical solutions, we also use the box trap, i.e., an infinitely deep rectangular potential well.

The subsequent presentations starts with the formulation of the system in Section 2, which also includes the above-mentioned estimate for the upshift of the MIM transition under the pressure of the confining potential, as well as a newly found exact DW solution for the system including the repulsive or attractive Pöschl-Teller potential. Section 3 reports approximate analytical results for DWs and MIM-transition point, obtained by means of a variational method. Comparison with numerical findings demonstrates high accuracy of the analytical approximation. In Section 4 we summarize findings for stable and unstable dynamical regimes in the system including the *miscibility management* (induced by the NM). The paper is concluded by Section 5.

II. THE SYSTEM WITH AND WITHOUT THE TRAPPING POTENTIAL

A. The estimate of the shift of the MIM transition point under the action of the parabolic trapping potential

The underlying system of one-dimensional GP equations for the component wave functions ψ_{\pm} of the binary condensate is written, in the scaled form, as

$$i\frac{\partial\psi_+}{\partial t} = -\frac{1}{2}\frac{\partial^2\psi_+}{\partial x^2} + (|\psi_+|^2 + g|\psi_-|^2)\psi_+ + \frac{\Omega^2}{2}x^2\psi_+ - \kappa\psi_-, \quad (2)$$

$$i\frac{\partial\psi_-}{\partial t} = -\frac{1}{2}\frac{\partial^2\psi_-}{\partial x^2} + (|\psi_-|^2 + g|\psi_+|^2)\psi_- + \frac{\Omega^2}{2}x^2\psi_- - \kappa\psi_+, \quad (3)$$

where Ω^2 is the strength of the trapping quadratic potential, and $g > 0$ is the relative strength of the inter-component repulsion, while the intra-component repulsion coefficient is scaled to be 1. Further, κ is the RC constant, which is fixed to be positive, as its negative value can be reversed by substitution $\psi_- \rightarrow -\psi_-$. It is convenient to fix $\kappa > 0$, as then stable two-component states, which provide for the minimum of the RC energy, correspond to identical signs of the components $\psi_{+,-}$.

To explore the MIM transition threshold in the framework of this system, one can look for a steady-state solution to Eqs. (2) and (3) with chemical potential μ ,

$$\psi_{\pm}(x, t) = e^{-i\mu t}u_{\pm}(x), \quad (4)$$

where real functions $u_{\pm}(x)$ satisfy the system of coupled stationary equations

$$\frac{1}{2}\frac{d^2u_+}{dx^2} + u_+(\mu - u_+^2 - gu_-^2) - \frac{\Omega^2}{2}x^2u_+ + \kappa u_- = 0, \quad (5)$$

$$\frac{1}{2}\frac{d^2u_-}{dx^2} + u_-(\mu - u_-^2 - gu_+^2) - \frac{\Omega^2}{2}x^2u_- + \kappa u_+ = 0. \quad (6)$$

In particular, a symmetric spatially even solution of Eqs. (5) and (6), $u_{\pm}(x) \equiv u_{\text{symm}}(x)$, $u_{\text{symm}}(-x) = u_{\text{symm}}(x)$, is produced by the single equation,

$$\frac{1}{2} \frac{d^2 u_{\text{symm}}}{dx^2} + u_{\text{symm}} [(\mu + \kappa) - (1 + g)u_{\text{symm}}^2] + \frac{\Omega^2}{2} x^2 u_{\text{symm}} = 0. \quad (7)$$

Stationary states produced by Eqs. (5) and (6) are characterized by the total norm,

$$N = \int_{-\infty}^{+\infty} \sum_{+,-} u_{\pm}^2(x) dx, \quad (8)$$

the corresponding energy of the system being

$$E = \int_{-\infty}^{+\infty} \left\{ \frac{1}{2} \sum_{+,-} \left[\left(\frac{du_{\pm}}{dx} \right)^2 + u_{\pm}^4 + \Omega^2 x^2 u_{\pm}^2 \right] + g(u_+ u_-)^2 - \kappa u_+ u_- \right\} dx. \quad (9)$$

The MIM transition is initiated by a small spatially odd perturbation, $\delta u(-x) = -\delta u(x)$, added to $u_{\text{symm}}(x)$:

$$(u_{\pm}(x))_{\text{perturbed}} = u_{\text{symm}}(x) \pm \delta u(x). \quad (10)$$

Substituting this expression in expression (9), the quartic terms give rise to the respective energy perturbation

$$(\delta E)_{\text{quart}} = 2 \int_{-\infty}^{+\infty} (3 - 2g) u_{\text{symm}}^2(x) (\delta u(x))^2 dx. \quad (11)$$

Without a detailed analysis of the solution, it is easy to conclude that other contributions to the energy perturbation, produced by the kinetic-energy, trapping-potential, and RC terms in Eq. (9), are negligible in comparison to one (11) under conditions

$$\kappa/N \ll \sqrt{\Omega} \ll N. \quad (12)$$

Then, also irrespective of the explicit form of functions $u_{\text{symm}}(x)$ and $\delta u(x)$, Eq. (11) predicts the MIM transition, i.e., the instability of the mixed state, following from $(\delta E)_{\text{quart}} < 0$, at $g > 3/2$. In comparison to the above-mentioned MIM condition (1), which in the present notation takes the form of $g > 1$, the expansion of the stability region of the mixed state from $g < 1$ to $g < 3/2$ is a result of the above-mentioned pressure applied to the binary BEC by the trapping potential.

In another parameter range, *viz.*, $\kappa \gg \Omega$, the effect of the trapping potential is negligible [4], and the boundary of the instability of the mixed state shifts from $g = 1$ to $g = 1 + 2\kappa/n_0$, where $n_0 \equiv 2u_{\pm}^2(x=0)$ is the total density of the binary BEC at the center, as shown below by Eq. (42).

B. An exact DW solution supported by the Pöschl-Teller potential

In the special case of $g = 3$ and $\Omega = 0$, an exact DW solution to Eqs. (5) and (6) was found in Ref. [32]:

$$\left\{ \begin{array}{l} \psi_+(x) \\ \psi_-(x) \end{array} \right\} (g = 3) = \frac{1}{2} e^{-it} \left\{ \begin{array}{l} \sqrt{1+\kappa} - \sqrt{1-\kappa} \tanh(\sqrt{1-\kappa} x) \\ \sqrt{1+\kappa} + \sqrt{1-\kappa} \tanh(\sqrt{1-\kappa} x) \end{array} \right\}, \quad (13)$$

in which the chemical potential is fixed as $\mu = 1$ [cf. Eq. (4)] by means of scaling. This solution, which exists for values of the RC coefficient

$$\kappa < \kappa_{\text{crit}} \equiv 1, \quad (14)$$

satisfies boundary conditions

$$u_+(x \rightarrow -\infty) = u_-(x \rightarrow +\infty) = \frac{1}{2} (\sqrt{1+\kappa} + \sqrt{1-\kappa}), \quad (15)$$

$$u_+(x \rightarrow +\infty) = u_-(x \rightarrow -\infty) = \frac{1}{2} (\sqrt{1+\kappa} - \sqrt{1-\kappa}). \quad (16)$$

Note that, for $g = 3$, condition (14) exactly agrees with the general existence condition (42), which is obtained below as a property of approximate analytical solutions. Our numerical analysis (not shown here in detail) *corroborates the full stability* of the DW produced by solution (13) for all values of κ from the existence range (14) (the stability of this solution was not explicitly studied in Ref. [32]).

A new result reported here is the possibility to extend the exact DW solution to the system of GP equations including the Pöschl-Teller potential [33]:

$$i\frac{\partial\psi_+}{\partial t} = -\frac{1}{2}\frac{\partial^2\psi_+}{\partial x^2} + (|\psi_+|^2 + g|\psi_-|^2)\psi_+ + \frac{W}{\cosh^2(\alpha x)}\psi_+ - \kappa\psi_-, \quad (17)$$

$$i\frac{\partial\psi_-}{\partial t} = -\frac{1}{2}\frac{\partial^2\psi_-}{\partial x^2} + (|\psi_-|^2 + g|\psi_+|^2)\psi_- + \frac{W}{\cosh^2(\alpha x)}\psi_- - \kappa\psi_+, \quad (18)$$

with specially selected values of the strength and width parameters, W and α :

$$W = \frac{3-g}{g-1} \frac{g-1-2\kappa}{4}, \quad \alpha = \sqrt{\frac{g-1-2\kappa}{2}}. \quad (19)$$

This potential can be readily implemented in the experimental setting for BEC with the help of an appropriately shaped laser beam illuminating the condensate [34].

Again fixing $\mu = 1$ by means of rescaling, the exact solution of Eqs. (17) and (18), with the potential's parameters chosen as per Eq. (19), is

$$\begin{cases} \psi_+(x) \\ \psi_-(x) \end{cases} = \frac{1}{2}e^{-it} \begin{cases} A - B \tanh(\alpha x) \\ A + B \tanh(\alpha x) \end{cases} \quad (20)$$

(cf. Eq. (13)), with

$$A = \sqrt{\frac{g-1+2\kappa}{g-1}}, \quad B = \sqrt{\frac{g-1-2\kappa}{g-1}}. \quad (21)$$

In the case of $g = 3$, this exact solution carries over into the above-mentioned one (13).

Note that, according to Eq. (19), the solution exists in the case of $g > 1 + 2\kappa$, and the potential is repulsive or attractive ($W > 0$ or $W < 0$, respectively), in the cases of $g < 3$ or $g > 3$. In fact, the repulsive potential, which helps to separate the two components, facilitates the creation of the DW, while the attractive potential makes the DW solution unfavorable. In accordance with this expectation, direct simulations of the coupled GPE (17)-(18) show that the repulsive potential supports stable DW, while the attractive one leads to its instability, as demonstrated in Fig. 1. In the latter case, the instability develops as spontaneous motion of the DW, which ends up with destruction of the DW upon collision with the border of the box trap, as shown by the spatiotemporal density plots in Figs. 1e), f).

C. The system without the trapping potential

Below, we address the system which does not include the trapping potential, but may include the action of the NM:

$$i\frac{\partial\psi_+}{\partial t} = -\frac{1}{2}\frac{\partial^2\psi_+}{\partial x^2} + (|\psi_+|^2 + g(t)|\psi_-|^2)\psi_+ - \kappa\psi_-, \quad (22)$$

$$i\frac{\partial\psi_-}{\partial t} = -\frac{1}{2}\frac{\partial^2\psi_-}{\partial x^2} + (|\psi_-|^2 + g(t)|\psi_+|^2)\psi_- - \kappa\psi_+, \quad (23)$$

where the NM is represented by the time-periodic modulation of the cross-repulsion coefficient:

$$g(t) = g_0 + \varepsilon \sin(\omega t). \quad (24)$$

The objective of the NM is to introduce ‘‘miscibility management’’ at frequency ω . In particular, this case is relevant if the constant part g_0 of the cross-repulsion coefficient g_0 is slightly greater than the critical value g_{MIM} at the MIM-transition point, and the NM amplitude is small, $\varepsilon \ll g_{\text{MIM}}$.

The Lagrangian of system (22)-(23) is

$$L = \int_{-\infty}^{+\infty} \mathcal{L} dx, \quad (25)$$

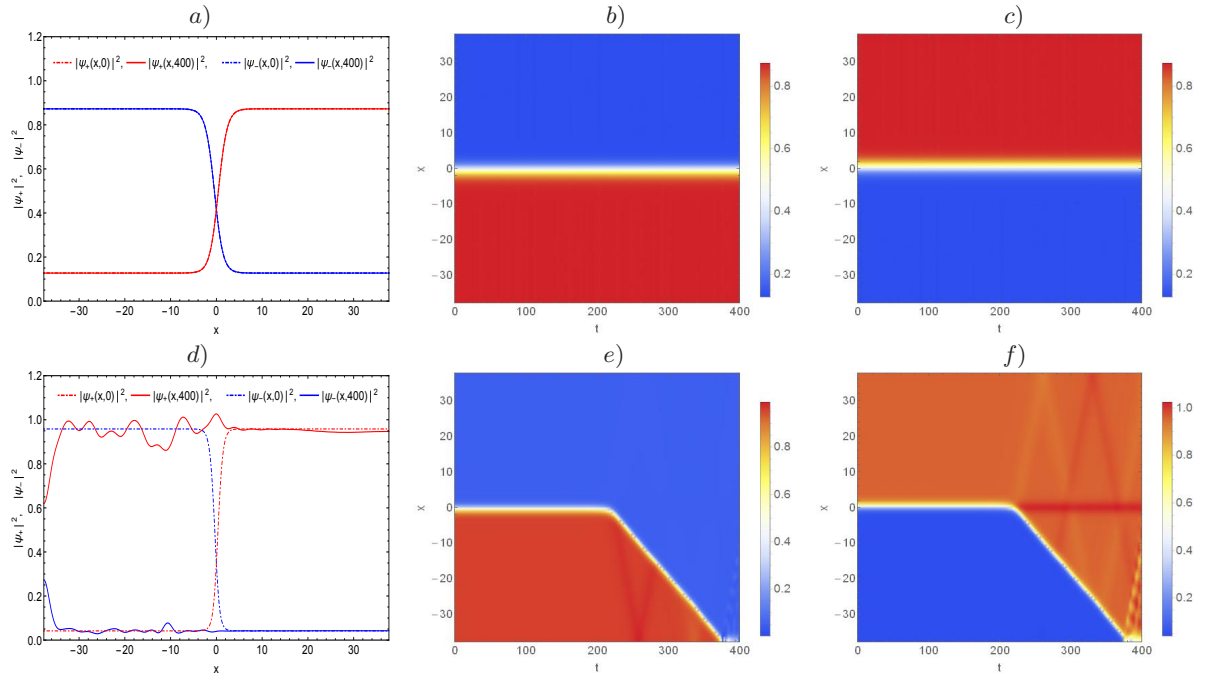


FIG. 1: a), d): Snapshots of the solutions produced by the simulations of the GP system (17)-(18) with the box trap, using the exact analytical solution (20) as initial conditions. The initial and final forms of the numerical solutions are represented by the dot-dashed and solid lines, respectively. b), c) The spatiotemporal evolution of components $|\psi_+(x, t)|^2$ and $|\psi_-(x, t)|^2$, initiated by the input with $\kappa = 0.5$, $g = 2.5$ [hence $W > 0$ in Eq. (19), which corresponds to the repulsive potential], shows stable propagation in the course of long time, $t = 400$. e), f): In contrast, the solution produced by the input with $\kappa = 0.5$, $g = 3.5$ (hence $W < 0$, making the potential attractive), is unstable. The unstable DW starts to move, eventually hitting the border of the box trap and thus disintegrating.

with the Lagrangian density

$$\mathcal{L} = \sum_{+,-} \left[\left(\frac{i}{2} \psi_{\pm}^* \frac{\partial \psi_{\pm}}{\partial t} + \text{c.c.} \right) - \frac{1}{2} \left| \frac{\partial \psi_{\pm}}{\partial x} \right|^2 - \frac{1}{2} |\psi_{\pm}|^4 \right] - g(t) |\psi_+|^2 |\psi_-|^2 + \kappa (\psi_+^* \psi_- + \text{c.c.}), \quad (26)$$

where both $*$ and c.c. stand for the complex conjugate. Below, the Lagrangian is employed to derive a variational approximation for dynamical DW states.

III. THE SINE-GORDON (SG) APPROXIMATION

A. The general analysis

In the case of the proximity to the MIM transition, a natural ansatz for an approximate solution is adopted as

$$\begin{Bmatrix} \psi_+ \\ \psi_- \end{Bmatrix} = \sqrt{n_0} \exp(-in_0 t) \begin{Bmatrix} (\cos \chi) \exp(+i\theta) \\ (\sin \chi) \exp(+i\theta) \end{Bmatrix}, \quad (27)$$

where n_0 is the background amplitude (eventually, one may set $n_0 \equiv 1$ by means of rescaling), while $\chi(x, t)$ and $\theta(x, t)$ are real phases, equations for which should be derived with the help of the Lagrangian representation of the system. For the stationary configurations, ansatz (27) coincides with the one introduced long ago in Ref. [31], which has $\theta = 0$.

The substitution of ansatz (27) in the Lagrangian density (26) yields the corresponding effective Lagrangian density:

$$\begin{aligned} \mathcal{L}_{\text{effect}} = & -\frac{n_0}{2} \cos(2\chi) \frac{\partial \theta}{\partial t} - \frac{n_0}{2} \left[\left(\frac{\partial \chi}{\partial x} \right)^2 + \left(\frac{\partial \theta}{\partial x} \right)^2 \right] \\ & - \frac{n_0^2}{8} [(3 + g(t)) + (1 - g(t)) \cos(4\chi)] + n_0 \kappa \sin(2\chi) \cos(2\theta). \end{aligned} \quad (28)$$

The Euler-Lagrange equations for χ and θ are produced by the application of the variational procedure to the Lagrangian produced by the effective density (28):

$$\sin(2\chi) \frac{\partial \theta}{\partial t} + \frac{\partial^2 \chi}{\partial x^2} + \frac{n_0}{2} (1 - g(t)) \sin(4\chi) + 2 \kappa \cos(2\chi) \cos(2\theta) = 0, \quad (29)$$

$$-\sin(2\chi) \frac{\partial \chi}{\partial t} + \frac{\partial^2 \theta}{\partial x^2} - 2 \kappa \sin(2\chi) \sin(2\theta) = 0. \quad (30)$$

In the case of the static configuration, with $g = \text{const}$, it is possible to drop θ from Eqs. (29) and (30), the remaining stationary version of Eq. (29) being, essentially, a stationary double-SG equation [35, 36]:

$$\frac{\partial^2 \chi}{\partial x^2} + \frac{n_0}{2} (1 - g) \sin(4\chi) + 2 \kappa \cos(2\chi) = 0. \quad (31)$$

In particular, if $\kappa = 0$, the obvious kink solution of the SG equation (31) corresponds to the DW, in terms of the underlying system (22)-(23), provided that the system is immiscible, i.e., $g - 1 > 0$:

$$\chi_{\text{DW}} = \arctan \left(\exp \left(\sigma \sqrt{2 n_0 (g - 1)} x \right) \right), \quad (32)$$

where $\sigma = \pm 1$ is the kink's polarity.

In the case of $g = \text{const}$, Eqs. (29) and (30) can be used to check the modulational stability of the uniformly mixed state, which corresponds to $\chi = \pi/4$ and $\theta = 0$, in the case of $g < 1$ (miscibility), and the modulational instability of the same state in the case of $g > 1$ (immiscibility). Indeed, taking the perturbed solution as

$$\chi = \pi/4 + \delta\chi(x, t) \quad \text{and} \quad \theta(x, t), \quad (33)$$

where $\delta\chi$ and θ are small perturbations, the linearization of Eqs. (29) and (30) for the perturbations yields the system

$$\begin{aligned} \theta_t + (\delta\chi)_{xx} + 2 n_0 (1 - g) \delta\chi - 4 \kappa \cdot \delta\chi &= 0, \\ -(\delta\chi)_t + \theta_{xx} - 4 \kappa \theta &= 0. \end{aligned} \quad (34)$$

The substitution of

$$\delta\chi(x, t), \theta(x, t) \sim \exp(iqx - i\omega t) \quad (35)$$

in Eqs. (34) gives rise to the dispersion relation for the modulational perturbations:

$$\omega^2 = 2n_0(1 - g)(q^2 + 4\kappa) + (q^2 + 4\kappa)^2. \quad (36)$$

Obviously, Eq. (36) gives rise to the stability and instability in the cases of $1 - g > 0$ and $1 - g < 0$, respectively, as expected. This dispersion relation is plotted in Fig. 2 for different values of the RC parameter κ .

B. The effect of the RC (Rabi coupling) and comparison of the SG approximation with numerical results

In the case of $g(t) = \text{const}$ and $\theta = 0$, the double-SG equations (31) can be written as follows:

$$\frac{d^2 \tilde{\chi}}{dz^2} = \sin \tilde{\chi} - K \cos \left(\frac{\tilde{\chi}}{2} \right) \equiv -\frac{dU_{\text{eff}}}{d\tilde{\chi}}, \quad (37)$$

$$U_{\text{eff}} = \cos \tilde{\chi} + 2K \sin \left(\frac{\tilde{\chi}}{2} \right), \quad (38)$$

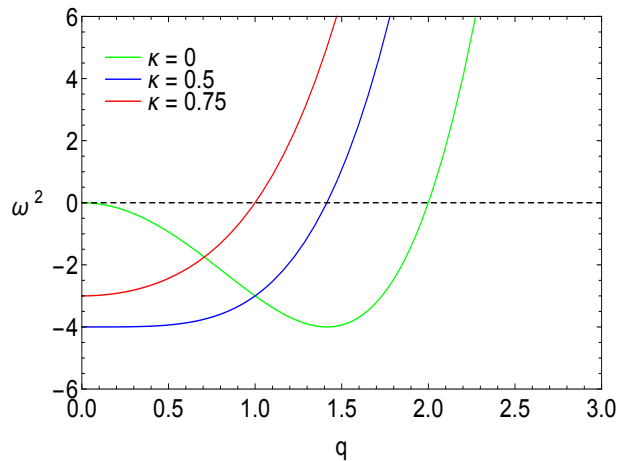


FIG. 2: The dispersion relation (36) for the modulational perturbations in the case of $n_0 = 1, g = 3$ and different values of the RC coefficient κ . The instability area ($\omega^2 < 0$) is shifted towards smaller wave numbers (q) as κ increases.

where $\tilde{\chi} \equiv 4\chi$, maxima of the effective potential (38) are attained at $\tilde{\chi}_0 = \pi + 4\pi n$, and

$$K \equiv 4\kappa/(n_0(g-1)), \quad (39)$$

$$z \equiv \sqrt{2n_0(g-1)}x. \quad (40)$$

Fixed-point solutions of Eq. (37), $\tilde{\chi} = \tilde{\chi}_0 = \text{const}$, are ones with

$$\sin\left(\frac{\tilde{\chi}_0}{2}\right) = \frac{K}{2}, \quad (41)$$

and $\cos(\tilde{\chi}/2) = 0$, i.e., $\tilde{\chi}_0 = \pi + 2\pi n$, where n is an arbitrary integer. The fixed point (41) exists at $K \leq 2$, i.e., if the RC strength takes values below the critical value:

$$\kappa < \kappa_{\text{crit}} = \frac{1}{2}n_0(g-1). \quad (42)$$

For the illustration of kink solutions of Eq. (37), it is instructive to look at plots of the effective potential (38) produced for $K < 2$ (Figs. 3 a,b) and $K > 2$ (Fig. 3 c). If condition (42) holds, Fig. 3 b) suggests the existence of

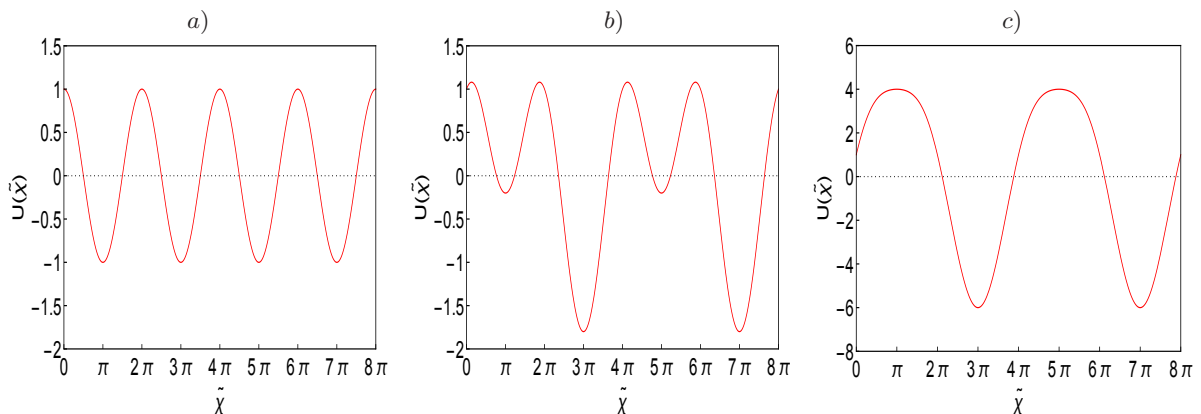


FIG. 3: The effective potential Eq. (38) for parameter values $n_0 = 1, g = 3$ and a) $K = 0$, b) $K = 0.4$, c) $K = 2.5$.

two species of DWs, “narrow” and “broad” ones. To obtain the respective solutions in the analytical form, we note that, for DW solutions, Eqs. (37) and (38) can be integrated once and thus reduced to the first-order one:

$$\frac{d\tilde{\chi}}{dz} = \pm \left(K - 2 \sin\left(\frac{\tilde{\chi}}{2}\right) \right). \quad (43)$$

Then, elementary exact solutions of Eq. (43) for the narrow and broad DWs are

$$\tilde{\chi}_{\text{DW}}^{(\text{narrow})} = \pi \mp 4 \arctan \left(\sqrt{\frac{1 - \frac{K}{2}}{1 + \frac{K}{2}}} \tanh \left(\sqrt{1 - \frac{K^2}{4}} \frac{z}{2} \right) \right), \quad (44)$$

$$\tilde{\chi}_{\text{DW}}^{(\text{broad})} = 3\pi \pm 4 \arctan \left(\sqrt{\frac{1 + \frac{K}{2}}{1 - \frac{K}{2}}} \tanh \left(\sqrt{1 - \frac{K^2}{4}} \frac{z}{2} \right) \right). \quad (45)$$

The solutions given by Eqs. (44) and (32) coincide in the absence of the RC term, $\kappa = 0$. If condition (42) does not hold, Fig. 3 c) suggests that Eq. (31) admits a kink solution, which connects states with $\chi = \pi/4$ and $\chi = 5\pi/4$. However, as it follows from Eq. (27), this kink is *not a DW*.

The accuracy and stability of the above approximate solutions can be verified by plugging them as initial conditions for the underlying GPE system. Figure 4 illustrates the time evolution of the inputs corresponding to the approximate analytical solutions (44) and (45), as produced by the simulations of Eqs. (22)-(23), using the following initial and boundary conditions (corresponding to the box trap, which confines the integration domain to $x \in [-L/2, +L/2]$, with the gradients of the wave functions at the edges of the box fixed to be the same as given by the approximate solution):

$$\psi_{\pm}(x, 0) = \left\{ \begin{array}{l} \cos \chi_{\text{DW}}(x) \\ \sin \chi_{\text{DW}}(x) \end{array} \right\}, \quad \left. \frac{\partial \psi_{\pm}(x, t)}{\partial x} \right|_{x \rightarrow \pm L/2} = \frac{d}{dx} \left\{ \begin{array}{l} \cos \chi_{\text{DW}}(x) \\ \sin \chi_{\text{DW}}(x) \end{array} \right\} \Big|_{x \rightarrow \pm L/2}. \quad (46)$$

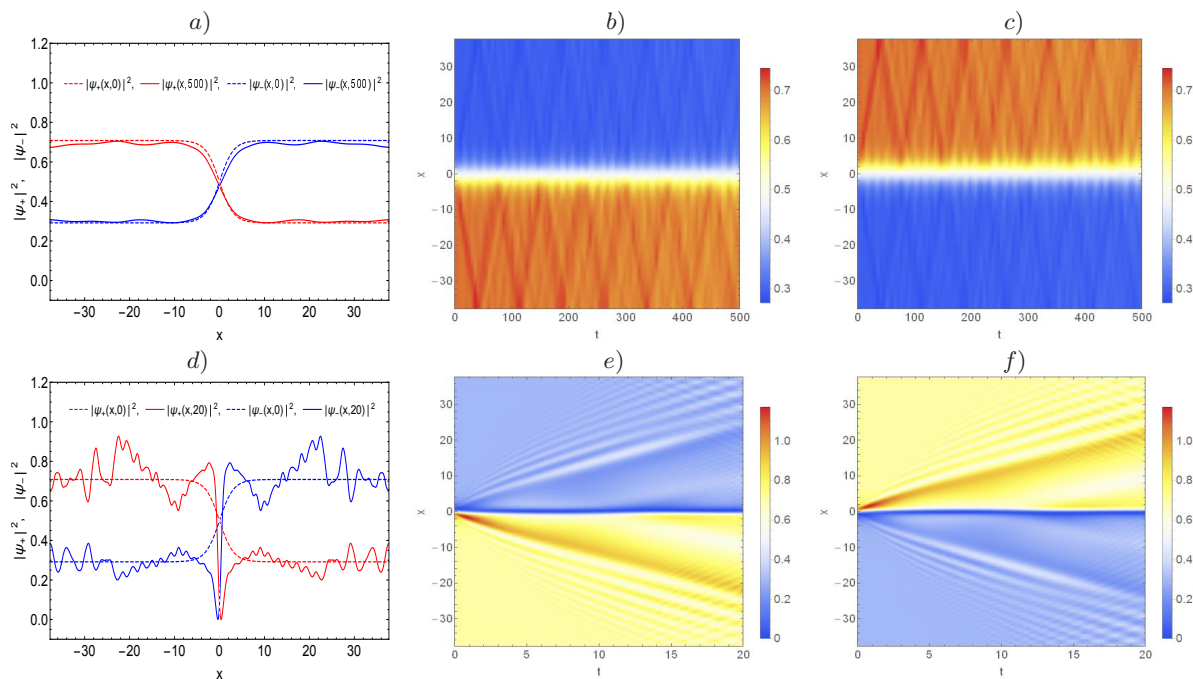


FIG. 4: a), d): Snapshots of the solutions produced by the simulations of the GP system (22)-(23) for the box trap with the approximate analytical solutions (44) and (45) used as initial conditions. The input and output of the numerical solutions are represented by the dashed and solid lines, respectively. a) The solution initiated by input (44) shows an effectively stable evolution over a long time, $t = 500$. d) In contrast, the solution produced by input (45) is unstable, breaking down very quickly, by $t = 20$. The density plots b), c) and e), f) show the corresponding spatiotemporal evolution of the components $|\psi_+(x, t)|^2$ and $|\psi_-(x, t)|^2$. In this case, the parameters are $n_0 = 1$, $g = 2.1$, $\kappa = 0.5$, and $K = 1.82$.

For the direct comparison of the approximate solutions with their numerically found counterparts, we have produced the ground-state solution of the system (22)-(23) on the ring, in the immiscibility regime, using the imaginary-time evolution method [37]. As said above, the ring geometry gives rise to the state with a pair of DWs located at diametrically opposite positions. In Fig. 5, the component densities $|\psi_{\pm}(x)|^2$ corresponding to the approximate analytical and numerical solutions are juxtaposed. The figure clearly shows high accuracy of the analytical approximation.

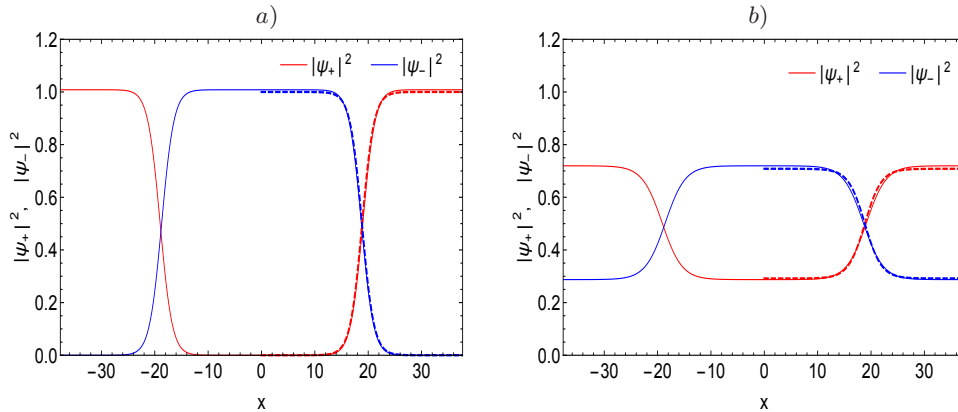


FIG. 5: Component densities $|\psi_+(x)|^2 = |\sin(\chi_{\text{DW}}(x))|^2$ and $|\psi_-(x)|^2 = |\cos(\chi_{\text{DW}}(x))|^2$ according to the approximate analytical solution (44) (dashed lines) and its numerically obtained counterpart in the ring configuration (solid lines) for the following parameter sets: a) $n_0 = 1$, $g = 1.1$, $\kappa = 0$; b) $n_0 = 1$, $g = 2.1$, $\kappa = 0.5$. With these parameter values, the system is close to the MIM transition, as specified by Eq. (42). The approximate solution slightly underestimates the width of the DW interface relative to the numerical solution.

IV. NUMERICAL SIMULATIONS OF THE MISCIBILITY MANAGEMENT

To explore the response of the DW structures to the application of the NM, defined as per Eq. (24), we numerically solved the system of Eqs. (22), (23), using either the approximate analytical solutions given by Eqs. (44) and (13), or numerically constructed solutions for the constant cross-repulsion coefficient, $g = g_0$, as initial conditions. For the ring-shaped system, the simulations were performed in real time by means of the split-step fast Fourier transform [38], with the periodic boundary conditions, $\psi_{\pm}(x = -L/2, t) = \psi_{\pm}(x = +L/2, t)$. For the box trap, where the periodic boundary conditions do not apply, the standard `NDSolve` routine of the Mathematica package has been employed, using the initial and boundary conditions as given by Eq. (46).

Below we consider the application of the NM in two cases: far from the MIM transition point ($g = 3$) and close to it ($g = 2.1$, as $g_{\text{cr}} = 2$ in this case) in the ring geometry. The perimeter of the ring is $L = 24\pi$, with centers of the two DWs initially placed at

$$x_{\text{center}} = \pm L/4. \quad (47)$$

In the former case ($g = 3$), our objective is to reveal the nonlinear resonance in the dynamics of the number of atoms on one side of the DW, driven by weak NM. In the latter case ($g = 2.1$), we are interested in observing the transition of the binary condensate from an immiscible to miscible state under the action of stronger NM, across the critical strength of the cross-repulsion coefficient, g . We fix a parameter set ($n_0 = 1$, $\kappa = 0.5$), for which $g_{\text{cr}} = 2$, according to Eq. (42).

A. The weak NM regime

Varying the strength of the cross-repulsion $g(t)$ alters the width of the DW's interface, with larger g corresponding to a narrower DW, and vice versa. The periodic variation of $g(t)$ leads to a similar variation in the number of atoms in the two components,

$$N_{\pm}(t) = \int_{L/4}^{L/2} |\psi_{\pm}(x, t)|^2 dx \quad (48)$$

on either side of the DW, due to the pulling or pushing the atoms from/to the phase boundary. The effect is more pronounced, as a resonant one, when the NM is applied at a frequency close to an eigenfrequency of the inner oscillations of the DW. The latter one can be identified from the results of simulations of a slightly perturbed system. In Fig. 6a) we show the oscillations of N_{\pm} corresponding to the quarter-ring on one side of the DW [see Fig. 4a) and Eq. (48)]. The oscillations are initiated by the quench of g from 3 to 3.3. Next, in Fig. 6b) we apply the NM defined as per Eq. (24), with $\omega = 2$, which is chosen as the eigenfrequency identified in Fig. 6a). The driven oscillations feature, in Fig. 6b), the signature of the nonlinear resonance [40], namely, periodic beatings of the oscillation amplitude due to periodic tuning to the resonance and detuning from it.

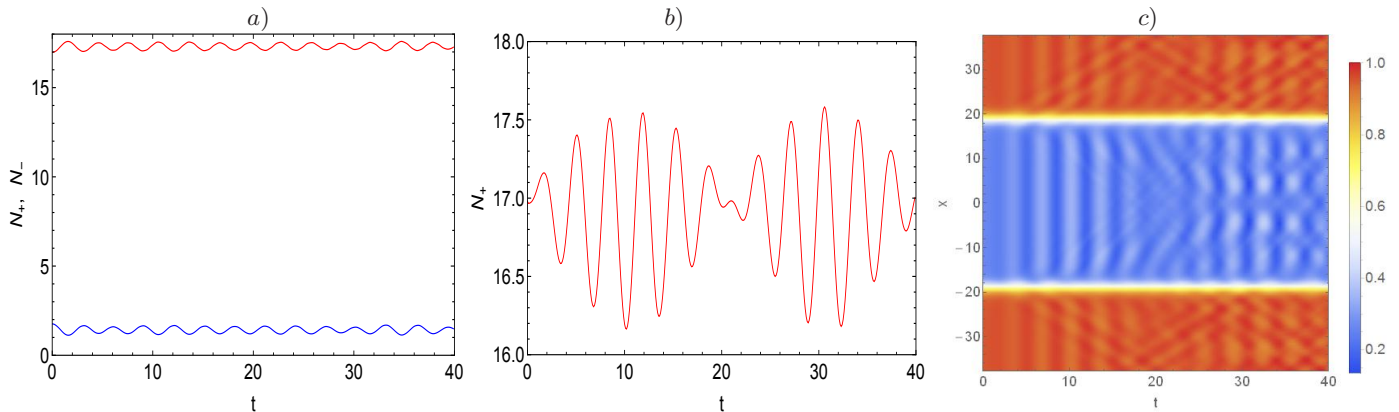


FIG. 6: a) Oscillations of the atom numbers N_{\pm} , defined according to Eq. (48), on one side of the DW interface. The oscillations are initiated by the sudden jump (quench) of the cross-repulsion coefficient from $g = 3$ to $g = 3.3$, at fixed $\kappa = 0.5$ with input (13). The simulations reveal the eigenfrequency of the inner oscillations $\omega_0 = 2$. b) Oscillations of the binary condensate driven by NM, in the form of Eq. (24) with $g = 3$, $\varepsilon = 0.1$ and $\omega = \omega_0 = 2$. The driven oscillations display beatings, which is the signature of the nonlinear resonance. c) The application of the NM gives rise to density waves, which are displayed here for component $\psi_+(x, t)$.

B. The management of the MIM transition in the ring geometry

The experimental realization of binary BECs in quasi-1D toroidal traps [39] motivates the study of DW-anti-DW pairs in the ring geometry. The advantage of this setting is that the absence of the external potential makes it possible to explore the phenomenology of the MIM transition in the “pure form”. DW-anti-DW complexes in the ring geometry were also considered for binary BECs with cubic-quintic nonlinearities and for Tonks–Girardeau binary gases in [27].

Here we address the effect of stronger NM, when the cross-repulsion coefficient, $g(t)$, periodically passes the critical value, g_{MIM} . To this end, we simulated the system (22)-(23), with the initial conditions corresponding to the numerically found ground states of the system with constant $g = g_0$. This ground state was, in turn, produced by means of the imaginary-time integration method, starting from the approximate analytical solution (44). Using the ring geometry, we set the two DWs, as said above, at points (47), with $L = 24\pi$. First, the initial DW profiles and their stability in the absence of NM are displayed in Fig. 7.

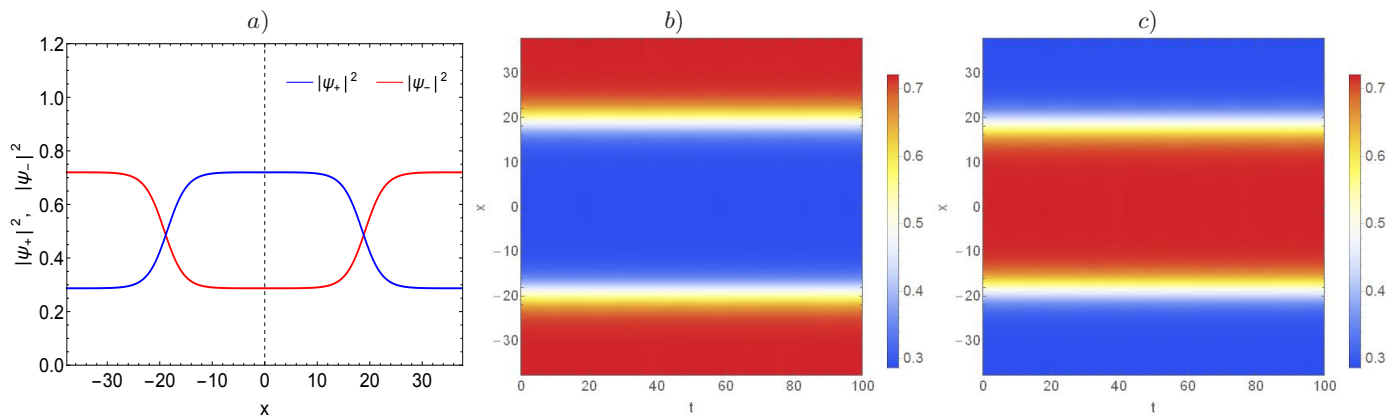


FIG. 7: a) The initial density profile for simulations of the evolution of the binary BEC in the ring-shaped setting is taken as the numerically constructed ground state. The stable evolution of the system is displayed by means of the density plots $|\psi_+(x, t)|^2$ in b) and $|\psi_-(x, t)|^2$ in c). The parameter values are $g = 2.1$, $\kappa = 0.5$, and the ring’s perimeter is $L = 24\pi$.

Next, we apply the NM, pursuant to Eq. (24), which drives periodic passage of $g(t)$ through the critical value for the MIM transition, $g_{\text{MIM}} = 2$, for $\kappa = 0.5$ [see Eq. (42)] and monitor the response of the DW states at different amplitudes ε of the periodic modulation. Figure 8 shows the outcomes demonstrating stable and unstable NM regimes, respectively. In the former case, the binary condensate remains immiscible, while in the latter case the stronger modulation induces a transition to miscibility, hence the DW structure is lost.

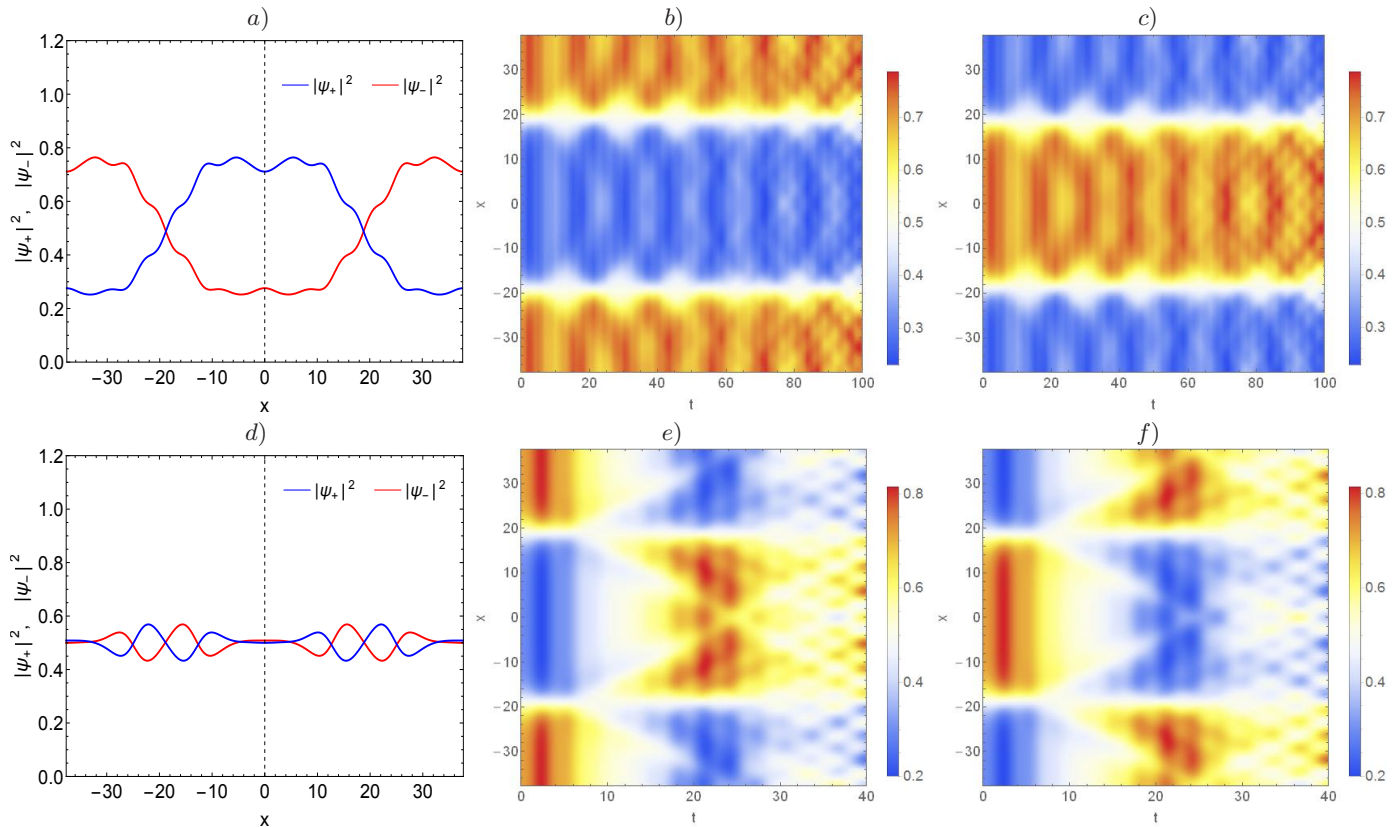


FIG. 8: The density profiles of the binary condensate evolving under the action of NM (24), with ω set equal to the above-mentioned internal eigenfrequency $\omega_0 = 2$, and $g_0 = 2.1$, $\kappa = 0.5$. Upper panels: Moderately strong NM with $\varepsilon = 0.2$ leads to $g(t)$ periodically passing the critical value of the MIM transition, $g_{\text{MIM}} = 2$. In this case, the NM generates small-amplitude density waves, preserving the DW structure. a) The component densities at final time $t = 100$. The spatiotemporal evolution of the density profiles of the components $|\psi_+(x, t)|^2$, b), and $|\psi_-(x, t)|^2$, c), shows their stability in the course of the evolution. Lower panels: Stronger NM with $\varepsilon = 0.4$ gives rise to the transition to miscibility (hence loss of the DW structure) around $t \simeq 10$. d) The component densities profiles just after the onset of the transition, at $t = 12$. e, f) The evolution of the component density patterns, $|\psi_{\pm}(x, t)|^2$.

Finally, the phase diagram for the MIM transition has been produced in the parameter plane (ε, ω) , as shown in Fig. 9. Naturally, the increase of ε favors the transition to the miscibility, while the increase of ω attenuates the effect of the time-periodic modulations and thus helps to keep the system in the immiscible phase.

V. CONCLUSIONS

In this work, we have obtained approximate analytical and numerical solutions for DWs (domain walls) in the binary BEC with self- and cross-repulsive nonlinearity; the system may also include the linear RC (Rabi coupling) between the components. The DW solutions, produced by the approximate method, based on the variational principle, and the respective prediction of the MIM (miscibility-immiscibility) transition, are in excellent agreement with their numerical counterparts. All the DW states are found to be stable. The approximate analytical solutions were also used as efficient inputs for producing the numerical solutions for the system's ground states, including those close to the MIM (miscible-immiscible) transition, by means of the imaginary-time propagation method. In addition, a particular exact DW solution was produced for the system including the Pöschl-Teller potential. The exact DW solution with the repulsive (attractive) Pöschl-Teller potential is found to be stable (unstable). The numerical results were chiefly obtained for the ring-shaped system, which carries a pair of DW and anti-DW, located at diametrically opposite positions. A crude analytical estimate was also reported for the shift of the MIM transition towards stronger cross-repulsion under the pressure of the trapping potential. Then, we addressed the system under the action of the miscibility management, imposed by the time-periodic modulation of the cross-repulsion strength, $g(t)$ (alias the nonlinearity management, NM). In the case of weak NM, when $g(t)$ does not pass through the MIM-transition point,

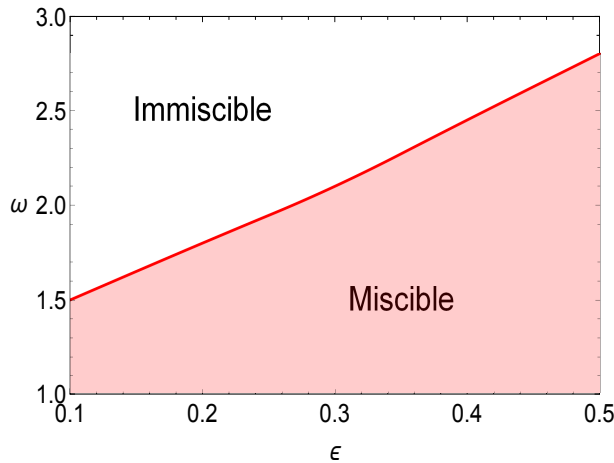


FIG. 9: The phase diagram for the MIM (miscibility-immiscibility) transition for the binary condensate under action of NM (24). The diagram is plotted in the (ϵ, ω) plane. Other parameters are $g_0 = 2.1$, $\kappa = 0.5$.

the system demonstrates excitation of a nonlinear resonance in the driven oscillations of the DW. Stronger NM, which leads to periodic passage of $g(t)$ across the MIM-transition point, may lead to a regime in which the stable DW survives. Eventually, strong NM pulls the system into the miscible state, and thus destroys DWs.

As an extension of the work, it may be interesting to include the linear spin-orbit coupling and Zeeman splitting between the two components of the binary condensate [41]. A promising possibility is to consider the miscibility management in two-dimensional systems.

Acknowledgments

We thank Prof. Hidetsugu Sakaguchi for a valuable discussion. B.B.B. acknowledges support from the State Budget of the Republic of Uzbekistan (Grant No. 2025 year award) and the Innovative Development Agency (Grant No. ALM-2023-1006-2528). The work of B.A.M. was supported, in part, by the Israel Science Foundation through grant No. 1695/22.

-
- [1] V. P. Mineev, The theory of the solution of two near-ideal Bose gases, *Zh. Eksp. Teor. Fiz.* 67, 263-272 (1974) [English translation: *Sov. Phys. – JETP* 40, 132-136 (1974)].
 - [2] E. Timmermans, Phase Separation of Bose-Einstein Condensates, *Phys. Rev. Lett.* 81, 5718-5721 (1998).
 - [3] C. J. Pethick and H. Smith, *Bose-Einstein condensation in dilute gases* (Cambridge University Press, Cambridge, 2002).
 - [4] M. I. Merhasin, B. A. Malomed, and R. Driben, Transition to miscibility in a binary Bose-Einstein condensate induced by linear coupling, *J. Phys. B: At. Mol. Opt. Phys.* 38, 877-892 (2005).
 - [5] F. Wang, X. Li, D. Xiong and D. Wang, A double species ^{23}Na and ^{87}Rb Bose-Einstein condensate with tunable miscibility via an interspecies Feshbach resonance, *J. Phys. B: At. Mol. Opt. Phys.* 49, 015302 (2016).
 - [6] C. Chin, R. Grimm, P. Julienne, and E. Tiesinga, Feshbach resonances in ultracold gases, *Rev. Mod. Phys.* 82, 1225 (2010).
 - [7] G. Roati, M. Zaccanti, C. D’Errico, J. Catani, M. Modugno, A. Simoni, M. Inguscio, and G. Modugno, ^{39}K Bose-Einstein Condensate with Tunable Interactions, *Phys. Rev. Lett.* 99, 010403 (2007).
 - [8] C. Cabrera, L. Tanzi, J. Sanz, B. Naylor, P. Thomas, P. Cheiney, and L. Tarruell, Quantum liquid droplets in a mixture of Bose-Einstein condensates, *Science* 359, 301-304 (2018).
 - [9] G. Semeghini, G. Ferioli, L. Masi, C. Mazzinghi, L. Wolswijk, F. Minardi, M. Modugno, G. Modugno, M. Inguscio, and M. Fattori, Self-bound quantum droplets of atomic mixtures in free space, *Phys. Rev. Lett.* 120, 235301 (2018).
 - [10] C. D’Errico, A. Burchianti, M. Prevedelli, L. Salasnich, F. Ancilotto, M. Modugno, F. Minardi, and C. Fort, Observation of quantum droplets in a heteronuclear bosonic mixture, *Phys. Rev. Res.* 1, 033155 (2019).
 - [11] B. Bakkali-Hassani, C. Maury, Y.-Q. Zou, É. Le Cerf, R. Saint-Jalm, P. C. M. Castilho, S. Nascimbene, J. Dalibard, and J. Beugnon, Realization of a Townes Soliton in a Two-Component Planar Bose Gas, *Phys. Rev. Lett.* 127, 023603 (2021).
 - [12] B. Bakkali-Hassani, C. Maury, S. Stringari, S. Nascimbene, J. Dalibard, and J. Beugnon, The cross-over from Townes solitons to droplets in a 2D Bose mixture, *New J. Phys.* 25, 013007 (2023).
 - [13] G. S. Rohrer, Grain boundary energy anisotropy: a review, *J. Materials Science*, 46, 5881-5895 (2001).

- [14] H. Lim, M. G. Lee, and R. H. Wagoner, Simulation of polycrystal deformation with grain and grain boundary effects, *Int. J. Plasticity* 27, 1328-1354 (2011).
- [15] P. Rudolph, Dislocation patterning and bunching in crystals and epitaxial layers - a review, *Cryst. Res. Tech.* 52, 1600171 (2017).
- [16] W. Yao, B. Wu, Y. Liu, Growth and grain boundaries in 2D materials, *ACS Nano* 14, 9320-9346 (2020).
- [17] U. Atxitia, D. Hinzke, and U. Nowak, Fundamentals and applications of the Landau-Lifshitz-Bloch equation, *J. Phys. D: Appl. Phys.* 50, 033003 (2017).
- [18] E. G. Galkina and B. A. Ivanov, Dynamic solitons in antiferromagnets, *Low Temp. Phys.* 44, 618-633 (2018).
- [19] S. Casado, W. Gonzalez-Vinas, H. Mancini, Testing the Kibble-Zurek mechanism in Rayleigh-Bénard convection, *Phys. Rev. E* 74, 047101 (2006).
- [20] M. A. Miranda, D. Laroze, W. Gonzalez-Vinas, The Kibble-Zurek mechanism in a subcritical bifurcation, *J. Phys. Cond. Matt.* 25, 404208 (2013).
- [21] M. C. Cross, Ingredients of a theory of convective textures close to onset, *Phys. Rev. A* 25, 1065-1076 (1982).
- [22] P. Manneville, Y. Pomeau, A grain-boundary in cellular structures near the onset of convection, *Phil. Mag. A* 48, 607-621 (1983).
- [23] V. Steinberg, G. Ahlers, D. S. Cannell, Pattern formation and wave-number selection by Rayleigh-Bénard convection in a cylindrical container, *Physica Scripta* 32, 534-547 (1985).
- [24] B. A. Malomed, A. A. Nepomnyashchy, M. I. Tribelsky, Domain boundaries in convection patterns, *Phys. Rev. A* 42, 7244-7263 (1990).
- [25] M. Haragus, A. Scheel, Grain boundaries in the Swift-Hohenberg equation, *Eur. J. Appl. Math.* 23, 737-759 (2012).
- [26] M. Haragus, G. Iooss, Bifurcation of symmetric domain walls for the Bénard-Rayleigh convection problem, *Arch. Rational Mech. Anal.* 239, 733-781 (2021).
- [27] G. Filatrella, B. A. Malomed, and M. Salerno, Domain walls and bubble droplets in immiscible binary Bose gases, *Phys. Rev. A* 90, 043629 (2014).
- [28] E. Nicklas, H. Strobil, T. Zibold, C. Gross, B. A. Malomed, P. G. Kevrekidis, and M. K. Oberthaler, Rabi flopping induces spatial demixing dynamics, *Phys. Rev. Lett.* 107, 193001 (2011).
- [29] B. A. Malomed, H. E. Nistazakis, D. J. Frantzeskakis, and P. G. Kevrekidis, Static and rotating domain-wall crosses in Bose-Einstein condensates, *Phys. Rev. A* 70, 043616 (2004).
- [30] S. Alama, L. Bronsard, A. Contreras, and D. E. Pelinovsky, Domain Walls in the Coupled Gross-Pitaevskii Equations, *Arch. Rational Mech. Anal.* 215, 579-610 (2015).
- [31] B. A. Malomed, Optical domain walls, *Phys. Rev. E* 50, 1565 (1994).
- [32] B. A. Malomed, New findings for the old problem: Exact solutions for domain walls in coupled real Ginzburg-Landau equations, *Phys. Lett. A* 422, 127802 (2022).
- [33] S. Flügge, *Practical Quantum Mechanics* (Springer-Verlag, Berlin, 1998).
- [34] A. L. Marchant, T. P. Billam, T. P. Wiles, M. M. H. Yu, S. A. Gardiner, and S. L. Cornish, Controlled formation and reflection of a bright solitary matter-wave, *Nature Comm.* 4, 1865 (2013).
- [35] D. K. Campbell, M. Peyrard, and P. Sodano, Kink-antikink interactions in the double sine-Gordon equation, *Physica D* 19, 165-205 (1986).
- [36] M. Wang and X. Li, Exact solutions to the double Sine-Gordon equation, *Chaos, Solitons & Fractals* 27, 477-486 (2006).
- [37] M. L. Chiofalo, S. Succi, M. P. Tosi, Ground state of trapped interacting Bose-Einstein condensates by an explicit imaginary-time algorithm, *Phys. Rev. E* 62, 7438 (2000).
- [38] S. K. Adhikari and P. Muruganandam, Bose-Einstein condensation dynamics from the numerical solution of the Gross-Pitaevskii equation, *J. Phys. B: At. Mol. Opt. Phys.* 35, 2831 (2002).
- [39] S. Beattie, S. Moulder, R. J. Fletcher, Z. Hadzibabic, Persistent currents in spinor condensates, *Phys. Rev. Lett.* 110, 025301 (2013).
- [40] R. Z. Sagdeev, D. A. Usikov, G. M. Zaslavsky, *Nonlinear Physics: From the Pendulum to Turbulence and Chaos* (Harwood Academic Publishers, 1988).
- [41] H. Zhai, Degenerate quantum gases with spin-orbit coupling: a review, *Rep. Prog. Phys.* 78, 026001 (2015).